Preliminary Study of Hydrodynamic Load on an Underwater Robotic Manipulator

Submitted: 21st June 2015; accepted: 12th August 2015

Waldemar Kolodziejczyk

DOI: 10.14313/JAMRIS_4-2015/28

Abstract:
The objective of this study was to obtain the hydrodynamic load on an underwater three-link robotic arm subjected to the different current speeds at several arm configurations under steady-state conditions. CFD simulations were performed in order to assess torque requirements when hydrodynamic effects have to be compensated by motors in order to maintain the position of the arm.

Keywords: *underwater manipulator, CFD, hydrodynamic load*

1. Introduction

Remotely operated manipulators are nowadays standard equipment for several underwater ROV (Remotely Operated Vehicles), as they offer underwater robots more flexibility and wider range of application, e.g. in picking up objects from the bed, joining parts, drilling… Industrial robots and manipulators operate in atmosphere which is much lighter than a rigid body. In underwater applications the density of water is comparable with the density of the manipulator and additional effects of hydrodynamic forces appearing in the system have to be taken into consideration, especially for fast, high performance manipulators, for which large hydrodynamic forces and torques may develop inducing unwanted motions [1]. The hydrodynamic effects on the manipulator are significant and affect the ability to achieve precise control [2]. The control of underwater robots and manipulators is, moreover, extremely difficult due to additional complex hydrodynamic loads including currents and wakes caused by nearby structures.

In a context of automatic control the hydrodynamic contribution to the forces acting on a system cannot be obtained from the continuity equation and the Navier-Stokes equations of motion, because they are ill-suited for on-line calculations. Hydrodynamic forces are taken into account through so called "added mass" contribution computed from the strip theory as a quotient of the hydrodynamic force divided by the acceleration of the body [3]. The added mass approach means that there is also an added Coriolis and added centripetal contribution.

Strip theory originates from potential flow background for 2D inviscid flows, and was extended semi-empirically to three dimensions [4]. Under the strip theory approach, the solid body is divided into multiple narrow slices, which can be considered as airfoils. Viscous effect of the fluid causes the drag and additional (beyond inviscid) lift force on the body, taken into consideration through simplified models including coefficients dependent on Reynolds number, without taking into account, for example, the configuration of the arm. However, there are results showing that drag and lift coefficients are not configuration independent [5].

The modeling of underwater manipulators has been studied in many works [4, 6, 7, 8, 9]. Underwater arms were modeled mostly as consisting of cylindrical links in order to simplify added mass, drag and lift forces calculations. Underwater manipulator in action changes its geometry during work, and consequently it is important to include the hydrodynamic effects of all links of the kinematic chain on the dynamics of the whole manipulator and the ROV.

The lumped approach to the hydrodynamic load on the underwater manipulators, mentioned in this section, is of limited accuracy and there are some controversies as to how added mass effect can be included, for example, for the wakes [10]. Fluid structure interactions (FSI) or computational fluid dynamics (CFD) methods enable more accurate results to be achieved. The fast development of computers, CFD methods and software make it possible to compute the results in more reasonable time than a short time ago, but naturally, not in real time, needed for control applications, for which, however, the obtained CFD results can be harnessed as useful data.

The objective of this paper was to examine the 3D steady-state hydrodynamics of the flow around the three-link manipulator placed in the current of incompressible water by using CFD methods. The present study concerned stationary three-link manipulator at different angles of the last link to the current. Seven robotic arm configurations were considered, subjected to the four different current speeds. It will enable us to compute the torques exerted on each joint of the manipulator at any configuration and at any velocity within the examined range as an interpolation function between values obtained, and consequently to make it possible to utilize results in control application for slow motion of the upper link or for slow current of water.

2. Modeling of the Flow Around the Robotic Arm. Case Study

The manipulator under consideration shown in Fig. 1 consists of three links with diameters of

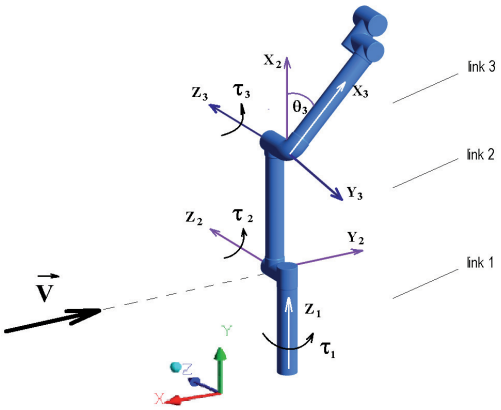

Fig. 1. Coordinate frame arrangement of the robotic arm (external and local reference frames)

8.4 cm. The lowest link is 0.43 m long, the middle one – 0.45 m, and the upper link has the cylindrical part of the length of 0.4 m. Two lower links of manipulator were kept unchanged. The modes of manipulator configurations are characterized by different arrangements of the third upper link inclined at seven angles θ_3 to the second (vertical) link: –135°, –90°, –45°, 0°, 45°, 90°, and 135°. Positive value of an angle θ_3 is measured in counter-clockwise direction with respect to the z_3 axis. The location of the arm with reference to the free stream of water is presented in Figs. 1 and 2. In a way, the angle θ_3 becomes then an indicator of arm position, relative to the velocity of the current which is oppositely directed to the *x* axis of the external system of coordinates (Fig. 1).

The computational domain in the shape of a box has been bounded only by the flat base of 8m long and 3m wide, considered as a solid wall. The arm is attached to the base in the middle of the width of the base at a distance of 2.5 m from free current inlet, as it is shown in Fig. 2. The 1/7th power law was used to specify turbulent velocity profile at the inlet to the domain. The other sides of computational domain of the height of 2.5 m were in contact with surrounding flowing water, i.e. the backflow to the domain may occur with the direction determined using the direction of the flow in the cell layer adjacent to the boundary.

Gulf Stream, Kuroshio, Agulhas, Brazil, and East Australian Currents flow at speeds up to 2.5 m/s. The strongest tidal current in the world, the Saltstraumen, flows at speed reaching 41 km/h (11.4 m/s). It was decided to limit the range of velocities in the present considerations to 1.5 m/s. Calculations were performed for four free current speeds: 0.1 m/s, 0.5 m/s, 1.0 m/s and 1.5 m/s. Reynolds numbers computed with respect to the links diameters and

a)

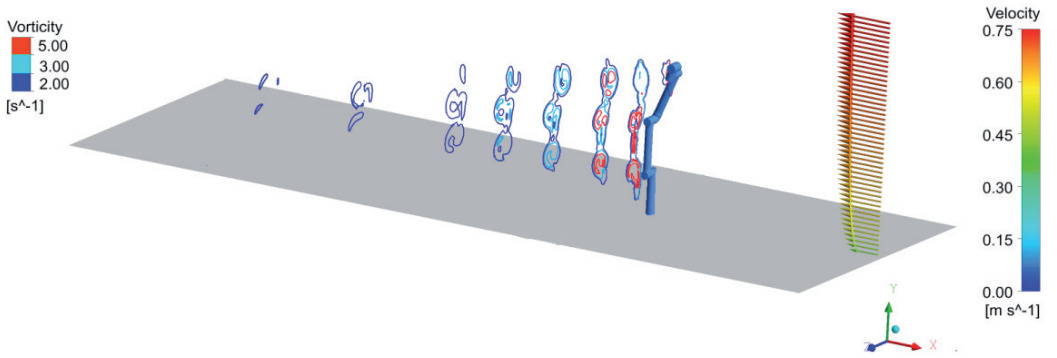

b)

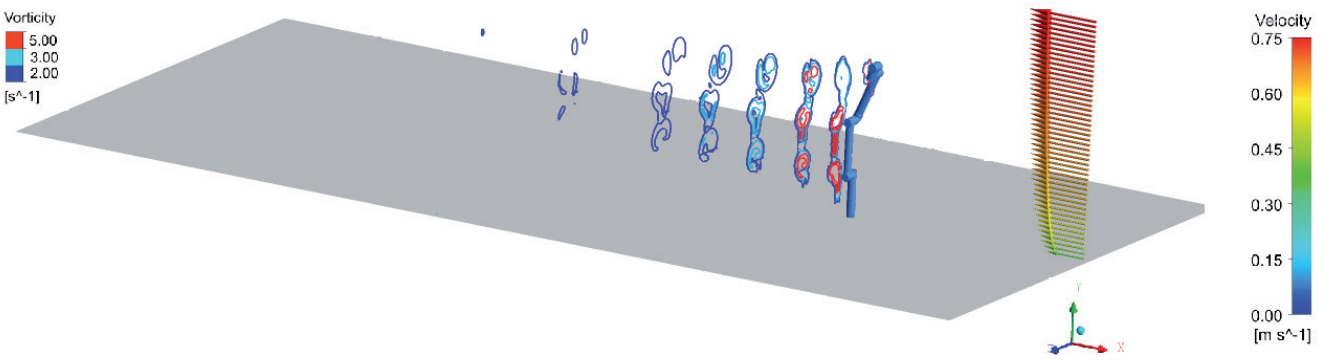

Fig. 2. The location of the manipulator in the computational domain for intermediate configuration mode described by θ_3 = –22.5° and vortex structures shedding from the arm at V = 0.75 m/s: a) for the computational domain of size of 8 m x 3 m x 2.5; b) for the reference domain of size of 11 m x 5 m x 3 m

current speeds were equal to 8 400, 42 000, 84 000 and 126 000, respectively.

The steady-state, incompressible viscous flow around a manipulator is described by the continuity equation and the Navier-Stokes equations of motion. The direct numerical simulations of N–S equations, where all the scales of the turbulent motion are resolved, exceed the capacity of currently existing computers, and then the governing equations have to be transformed to the Reynolds Averaged Navier-Stokes (RANS) equations:

$$\frac{\partial u_i}{\partial x_i} = 0; \tag{1}$$

$$\rho u_j \frac{\partial u_i}{\partial x_j} = -\frac{\partial p}{\partial x_i} + \frac{\partial}{\partial x_j}\mu\left(\frac{\partial u_i}{\partial x_j} + \frac{\partial u_j}{\partial x_i}\right) + \rho \frac{\partial\left(-\overline{u_i' u_j'}\right)}{\partial x_j}, \tag{2}$$

where x_i, x_j are the Cartesian coordinates, u_i, u_j are mean velocity components in *X*, *Y* and *Z*, directions, u'_i, u'_j are the fluctuating velocity components, ρ is the density of fluid, p is the pressure, μ – the viscosity.

The terms $(-\rho\overline{u_i' u_j'})$, called the Reynolds stresses, must be modeled in order to close the problem. Usually they are modeled utilizing the Boussinesq hypothesis:

$$-\rho\overline{u_i' u_j'} = \mu_t\left(\frac{\partial u_i}{\partial x_j} + \frac{\partial u_j}{\partial x_i}\right) - \frac{2}{3}\left(\rho k + \mu_t \frac{\partial u_k}{\partial x_k}\right)\delta_{ij}, \tag{3}$$

where μ_t is the turbulent viscosity, k – turbulence kinetic energy, and δ_{ij} is the Kronecker's delta.

The ways in which turbulent viscosity μ_t and turbulent kinetic energy k are computed are called models of turbulence. In the present study the standard k–ε model of turbulence was applied, for its robustness, economy, and reasonable accuracy for fully turbulent flows. The standard k–ε model is combined of two transport equations for the turbulence kinetic energy (k) and its dissipation rate (ε):

$$\frac{\partial}{\partial x_i}(\rho k u_i) = \frac{\partial}{\partial x_j}\left[\left(\mu + \frac{\mu_t}{\sigma_k}\right)\frac{\partial k}{\partial x_j}\right] + G_k - \rho\varepsilon, \tag{4}$$

and

$$\frac{\partial}{\partial x_i}(\rho\varepsilon u_i) = \frac{\partial}{\partial x_j}\left[\left(\mu + \frac{\mu_t}{\sigma_\varepsilon}\right)\frac{\partial \varepsilon}{\partial x_j}\right] + C_{1\varepsilon}\frac{\varepsilon}{k}G_k - C_{2\varepsilon}\rho\frac{\varepsilon^2}{k}, \tag{5}$$

where $C_{1\varepsilon}$ = 1.44, $C_{2\varepsilon}$ = 1.92, σ_k = 1.0 and σ_ε = 1.3 are the model constants. The term G_k represents the generation of turbulence kinetic energy due to the mean velocity gradients evaluated as:

$$G_k = \mu_t S^2, \tag{6}$$

where $S = \sqrt{2S_{ij}S_{ij}}$ is the modulus of the mean rate-of-strain tensor.

a) ***b)***

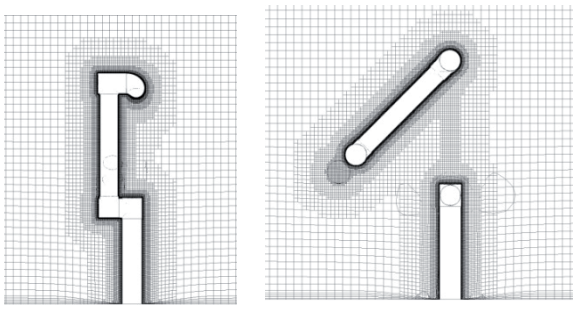

Fig. 3. The examples of computational grid close to the manipulator for configuration mode described by θ_3 = 135°

In this model the turbulent viscosity is computed as follows:

$$\mu_t = \rho C_\mu \frac{k^2}{\varepsilon}, \tag{7}$$

where C_μ = 0.09 is a constant.

The ANSYS CFD (ANSYS Inc., Canonsburg, Pennsylvania, USA) software was used to perform simulations. For the computational domain with different manipulator configurations the set of eight meshes of approx. 9 500 00 ÷ 11 500 000 elements were generated using cut-cell method. Figure 3 shows an example of the computational grid near the manipulator for configuration mode described by θ_3 = 135°.

Simulations were carried out in Parallel Fluent 16.0 (which implements the control volume method) with twelve parallel processes by utilizing the SIMPLE algorithm (Semi-Implicit Method for Pressure Linked Equations), a second order spatial pressure discretization and second order upwind discretization schemes for momentum equations and for the model of turbulence.

This research has been focused on the calculations of torques exerted by the current of water about three z axes in local reference frames assigned to the arm links, as they are shown in Fig. 1. Going from top to bottom, the torque τ_3 was calculated taking into account pressure and shear stress distributions along the surface of upper link about z_3 axis. The torque τ_2 includes hydrodynamic effects (due to pressure and shear stresses) on the two upper links with respect to z_2 axis and the torque τ_1 – describes the action of water on the whole manipulator about z_1 axis. They can be considered as joint torques experienced by the manipulator placed into the current of water and which have to be compensated by motors in order to maintain the positions of the links.

Moments (torques) of pressure and viscous forces along a specified axis are determined as the dot products of a unit vector in the direction of the axis and the net values of the moments computed by summing the cross products of the position vector of the pressure and viscous forces origins with respect to the moment center with the pressure and viscous force vectors for each boundary cell-face belonging to the discretized surface of the arm.

Table 1. Domain dependence study

Domain size l×w×h [m×m×m] Number of cells N		Torques [N m]			Domain dependence factor [%]		
		τ_1	τ_2	τ_3	δ_1	δ_2	δ_3
1	8×3×2.5 11 450 290	–1.048	10.259	4.375	5.75	2.50	2.30
2	6×3×2.5 10 898 000	-0.931	10.881	4.666	6.05	3.41	4.19
3	11×3×2.5 12 227 519	-0.945	10.429	4.525	4.64	0.88	1.05
4	8×4×3 12632671	-0.941	10.490	4.562	5.05	0.30	1.88
5	11×5×3.5 15 297 509	-0.991	10.522	4.478			

Table 2. Grid independence study

Sl. No. *i*	Number of cells *N*	Torques [N m]			Grid independence factor [%]		
		τ_1	τ_2	τ_3	δ_1	δ_2	δ_3
1	2992942	-1.455	11.949	3.836	3.00	1.79	2.70
2	5065890	-1.494	11.556	3.696	0.40	1.55	1.04
3	6142455	-1.506	11.561	3.714	0.40	1.51	0.56
4	9751800	-1.500	11.738	3.735			

In order to investigate the effect of the size of the domain and the computational mesh resolution on the results of simulations the domain and grid independence study were conducted.

Domain dependence was checked quantitatively in a series of simulations carried out for particular arm configuration described by $\theta_3 = -22.5°$, for current speed V = 0.75 m/s and for different sizes of the domain: the length l, the width w and the height h shown in Tab. 1. Domain dependence factor was defined as:

$$\delta_j(i) = 100 \left| \frac{\tau_j(i) - \tau_j(r)}{\tau_j(r)} \right|, \qquad (8)$$

where τ_1, τ_2, τ_3 are torques obtained for different sizes of the domain, j is an indicator of the torque (1, 2 or 3), i – stands for a serial number of the domain (see Tab. 1), $\tau_j(r)$ is the "j" torque computed for the reference "r = 5" domain of maximum size 11 m×5 m×3.5 m. The domain selected for computation is indicated by No. 1 in Tab. 1 (size: 8 m×3 m ×2.5 m). The relative difference of torques for actual domain computed with reference to those obtained for the domain of maximum size was equal to 5.75% for τ_1, and was equal or less than 2.5% for τ_2 and τ_3. The most important geometrical feature of the domain was its length. It was selected as a compromise between the need to capture all the structures of the flow and the capacity of available computers. Vortex structures (Fig. 2) forming the wakes shedding from the manipulator for actual computational domain and for the reference one are very similar in shape and the length of the wake is almost the same (vorticity contours were drawn at the same locations in both cases), so it can be stated that the actual computational domain was made long enough to capture all the features of the flow.

Grid independence study was performed for the position of the arm indicated by θ_3 = 45° and for current speed V = 1m/s, comparing resulting torques τ_1, τ_2, τ_3, obtained for meshes of different resolutions, as it is shown in Tab. 2. Grid independence factor was defined in the same way as domain dependence factor (8), except that i – stands for a serial number of the mesh (Tab. 2), $\tau_j(r)$ is the "j" torque computed for the reference "r = 4" grid of maximum number of cells. As can be seen in Tab. 2, grid independence factor constantly decreases with increasing number of cells and for two finest meshes of cell numbers 6142455 and 9751800, the relative differences of the torques were less than 1.6%. In order to better capture the flow structures, the finest mesh (No. 4) was selected and, consequently, the number of cells for all computational cases was kept in the range of 950000 ÷ 11500000 cells.

3. Results and Discussion

The results of calculations are summarized in Tab. 3 for four velocities of the current and for seven configuration modes of the robotic arm. The obvious conclusion is that the largest torques appear for the greatest current speed (1.5 m/s), but the effect of configuration mode of the manipulator is not so evident. All the configurations of the manipulator induce negative moments about the lower link (z_1 axis). The highest negative τ_1 is observed for θ_3 = –45°and –135°, that is when the upper arm is inclined upstream at an angle of 45° to the top or to the bottom of the free stream.

All the torques τ_2 computed from pressure and shear stress distributions along two upper links are positive. The highest τ_2 are located in the range of θ_3 between –45° and +45°. The lowest torque τ_2 appears for θ_3 = –135°, that is when the upper link is inclined upstream to the bottom. The torque τ_3 changes its direction determined by the position of the upper link and the current speed. It remaines positive in almost all cases for θ_3 between –45° and +90°, and negative in almost all cases for θ_3 = –90°, –135° and 135°.

The obtained magnitudes of joint torques can be used as interpolation points in procedures generating the interpolation functions for computing τ_1, τ_2 and τ_3 at intermediate values of current speeds and in inter-

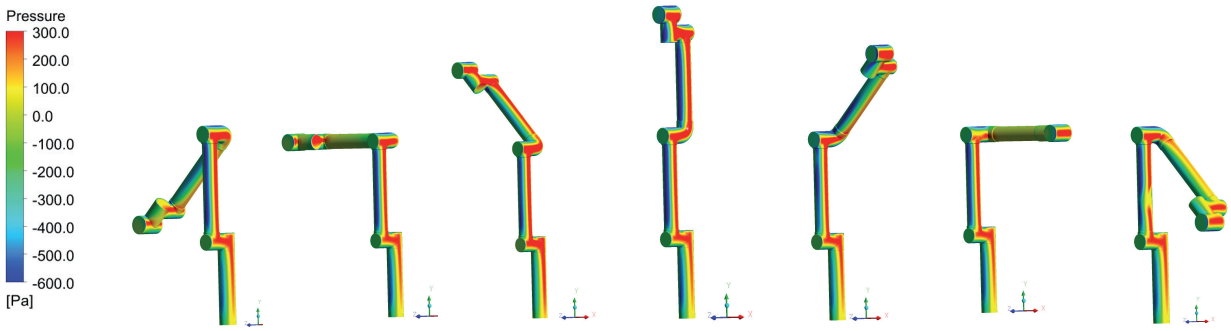

Mode: a) θ_3 = 135° b) θ_3 = 90° c) θ_3 = 45° d) θ_3 = 0° e) θ_3 = -45° f) θ_3 = –90° e) θ_3 = -135°

Fig. 4. Gauge pressure distribution on the surface of the arm at speed of the current V = 1 m/s

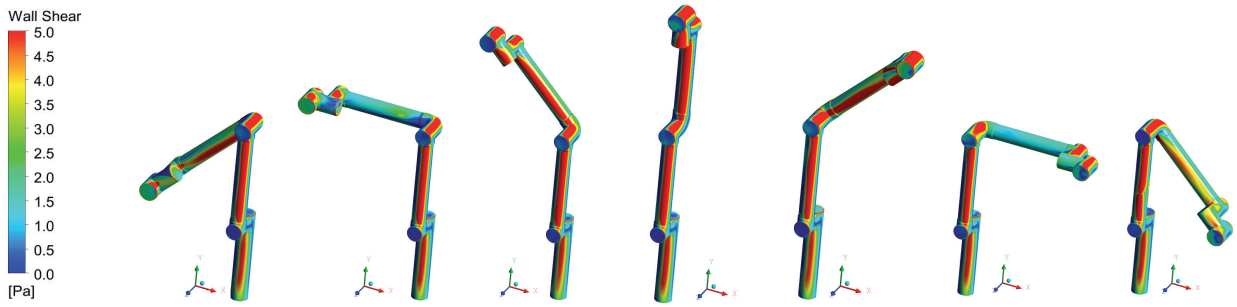

Mode: a) θ_3 = 135° b) θ_3 = 90° c) θ_3 = 45° d) θ_3 = 0° e) θ_3 = –45° f) θ_3 = –90° e) θ_3 = –135°

Fig. 5. Shear stress distribution on the surface of the arm at speed of the current V = 1 m/s

mediate positions of the upper link. The distributions of joint torques in the space created by an angle θ_3 and velocity V of the current are shown in Figs. 6÷8. In figure 8 the areas of positive and negative moments were separated by thicker zero-torque isolines in order to show the relationship between them better and to indicate, when the motor has to change the direction of rotation.

The results of the present calculations allow assessing how much the hydrodynamic forces impact the torques required to be supplied by motors. In control applications the joint moments to be compensated due to hydrodynamic loads can be obtained by using simple interpolation procedures utilizing, for example, bicubic 2D splines [11].

The hydrodynamic torques is caused by pressure and shear stress distributions along the surface of the manipulator links. The effect of pressure is much higher than that of shear stresses. Figures 4 and 5 present the pressure and wall shear contours on the robotic arm, obtained for speed current V = 1 m/s and for all considered configuration modes. The contours are seen from the direction different in each figure and most convenient in each case. The external system of coordinates placed near the arm indicates the position of the manipulator in relation to the current.

Generally, the pressure is at its highest on the surfaces that are facing the current, and at its lowest on sides' transversal to the current and on the sharp edges of the arm, that is in regions of the maximum velocity gradients and separation. They are also the areas of the maximum shear stresses as it is clearly seen in Figs. 4 and 5. The biggest pressure difference for current speed V = 1m/s was found to be approx. equal to 1200 Pa. Maximum values of positive gauge pressure were found to be about 350÷450Pa (depending on the configuration mode) on the upstream sides of the arm, and the greatest absolute value of the negative gauge pressure rose to about 1000Pa on the sharp edges of the third link, where the maximum velocities and shear stresses appeared (approx. 15 N/m^2).

Wake formation in the flow around the manipulator strongly affects the hydrodynamic forces and torques. The strip theory used to compute the added mass, drag and lift forces oversimplifies the flow patterns and interaction effects caused by changing geometry of the arm during its work. In the present simulations different wake patterns were observed depending on different configurations. One of them, for the intermediate configuration θ_3 = –22.5° and for current speed V = 0.75m/s, is presented in Fig. 2 as contours of vorticity shedding from the links.

4. Conclusions

CFD analysis has been performed to investigate the flow around the three-link manipulator placed in the current of water. ANSYS Fluent software was used to predict the flow structure near the manipulator arm and to compute the hydrodynamic torques in several configurations of the underwater manipulator and for several velocities of the current flowing around it.

The hydrodynamic torques computed in this study may be applied as external loads to dynamic model of the manipulator in order to obtain more accurate and

Table 3. Joint torques due to hydrodynamic effects

Configuration mode		τ_1 [Nm]				τ_2 [Nm]				τ_3 [Nm]			
		V [m/s]				V [m/s]				V [m/s]			
		0.1	0.5	1.0	1.5	0.1	0.5	1.0	1.5	0.1	0.5	1.0	1.5
θ_3	135°	-0.010	-0.226	-0.717	-0.847	0.036	0.982	4.046	8.649	-0.009	-0.284	-1.912	-4.154
	90°	-0.008	-0.161	-0.955	-1.682	0.028	1.023	3.938	9.371	-0.005	0.093	0.262	1.249
	45°	-0.006	-0.301	-1.500	-3.511	0.084	2.604	11.738	26.213	0.021	0.798	3.735	8.039
	0°	-0.009	-0.252	-1.186	-2.804	0.134	3.631	16.629	39.232	0.050	1.373	6.034	13.931
	-45°	-0.014	-0.474	-2.414	-4.937	0.128	4.099	16.708	39.146	0.067	1.875	7.372	17.622
	-90°	-0.005	-0.143	-0.613	-1.264	0.027	0.804	3.846	7.985	-0.002	-0.042	0.030	-0.362
	-135°	-0.009	-0.281	-1.463	-4.226	0.004	0.136	1.199	3.919	-0.052	-1.504	-5.873	-9.732

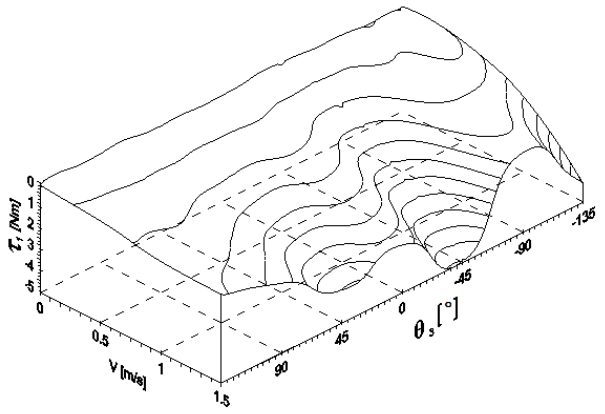

Fig. 6. Interpolation surface for joint torque τ_1

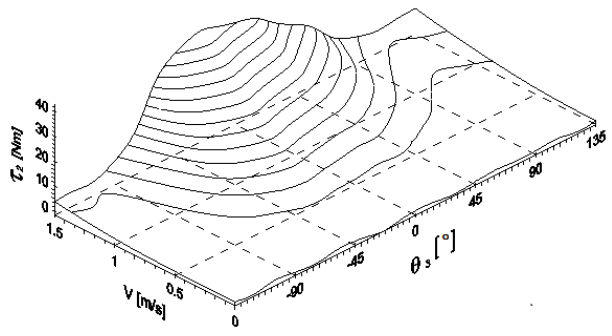

Fig. 7. Interpolation surface for joint torque τ_2

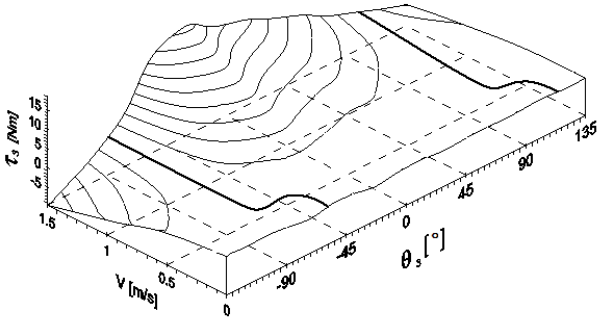

Fig. 8. Interpolation surface for joint torque τ_3

Table 4. Joint torques in intermediate position of the arm and at intermediate current speed V = 0.75 m/s

	τ_1 [Nm]	τ_2 [Nm]	τ_3 [Nm]
CFD calculations	-1.048	10.258	4.375
Interpolation - bicubic 2D splines	-1.029	9.667	4.012
Relative difference	0.018	0.058	0.083

more realistic simulation of the manipulator motion. The results can be applied in robotic models to define control strategies that will take into account the hydrodynamic forces computed for different modes of arm configurations and velocities of current with application of interpolation functions. In the table 4 the joint torques computed for an intermediate position of the last link (θ_3 = −22.5°), when the upper arm is slightly inclined upstream as one can see in Fig. 2, and for intermediate current speed V = 0.75 m/s by using the CFD approach and bicubic 2D splines [11] are presented. Relative differences between CFD calculation and the values interpolated from the data presented in Tab. 3 are less than 10%.

There is also a possibility of obtaining the lift and drag forces and consequently added mass for each link of the manipulator more accurately than from the strip theory and utilizing them in modeling of the dynamics of manipulator.

Underwater manipulators are usually sturdier than presented one, symmetrical in shape in most cases, and with, usually, not cylindrical links. The manipulator under investigation is based on UR 5 with cylindrical links, and it is non-symmetrical in shape. These features may give us many benefits in our investigations. Firstly, non-symmetrical shape of the arm allows us to investigate the effect of hydrodynamic load in more general way. Then cylindrical links enable us (in future works) to compare the hydrodynamic loads computed through numerical approach with results obtained via standard added mass calculations, which are more suited for links of robotic arm shaped cylindrically.

This paper presents just the first step in understanding of hydrodynamic loads on the

underwater robotic arm via numerical simulations, because it concerns only on the steady-state flow around different configurations of the last link of the arm. In the future, we will focus on the determination how the motion of the arm may affect the magnitude and direction of joint torques which in turn may give us information about the range of current speeds and velocities of the last link for which the flow might be considered as steady-state.

ACKNOWLEDGEMENTS

This work was supported by the Bialystok University of Technology under the grant No. S/WM/1/2012.

AUTHOR

Waldemar Kołodziejczyk – Bialystok University of Technology, Faculty of Mechanical Engineering, Department of Automatic Control and Robotics, ul. Wiejska 45 c, 15-351, Bialystok, Poland. E-mail: w.kolodziejczyk@pb.edu.pl.

REFERENCES

[1] Antonelli G., *Underwater Robots*, Springer Tracts in Advanced Robotics, Second edition, Springer, 2006.

[2] Farivarnejad H., Moosavian S.A., "Multiple Impedance Control for object manipulation by a dual arm underwater vehicle-manipulator system", *Ocean Engineering*, vol. 89, 2014, 82–98. DOI: 10.1016/j.oceaneng.2014.06.032.

[3] Fossen T.I., *Guidance and Control of Ocean Vehicles*, John Wiley & Sons, Chichester, United Kingdom, 1994.

[4] McLain T.W., Rock S.M., "Development and Experimental Validation of an Underwater Manipulator Hydrodynamic Model", *The International Journal of Robotics Research*, vol. 17, 1988, 748–759.

[5] Leabourne K.N., Rock S.M., "Model Development of an Underwater Manipulator for Coordinated Arm-Vehicle Control". In: *Proceedings of the OCEANS '98 Conference*, Nice, France, no. 2, 1998, 941–946.

[6] Richard M.J., Levesque B., "Stochastic dynamic modelling of an open-chain manipulator in a fluid environment", *Mech. Mach. Theory*, vol. 31, no. 5, 1996, 561–572.

[7] Rivera C., Hinchey M., "Hydrodynamics loads on subsea robots", *Ocean Engineering*, vol. 26, no. 8, 1999, 805–812. DOI: 10.1016/S0029-8018(98)00031-6.

[8] Vossoughi G.R., Meghdari A., Borhan H., "Dynamic modeling and robust control of an underwater ROV equipped with a robotic manipulator arm". In: *Proceedings of 2004 JUSFA, @004 Japan-USA Symposium on Flexible Automation*, Denver, Colorado, July 19–21, 2004.

[9] Pazmino R.S., Garcia C.E., Alvarez Arocha C., Santoja R.A., "Experiences and results from designing and developing a 6DOF underwater parallel robot", *Robotics and Autonomous System*, 59, 2011, 101–112.

[10] Williamson C.H.K., Govardhan R., "A brief review of recent results in vortex-induced vibrations", *Journal of Wind Engineering and Industrial Aerodynamics*, vol. 96, no. 6–7, 2008, 713–735. DOI: 10.1016/j.jweia.2007.06.019.

[11] Press W.H., Teukolsky S.A., Vetterling W.T., Flannery B.P., *Numerical recipes in C, The art of scientific computing*, Second edition, Cambridge University Press, 1992.